

1

## Effect of leading edge cut on the aerodynamics of ram-air parachutes

3

R. Balaji, S. Mittal<sup>\*,†</sup> and A. K. Rai

5

*Department of Aerospace Engineering, Indian Institute of Technology, Kanpur, UP 208 016, India*

### SUMMARY

7 The effect of the configuration of leading edge cut on the aerodynamic performance of ram-air parachutes  
8 is studied via two-dimensional flow simulations. The incompressible Reynolds-averaged Navier–Stokes  
9 equations, in primitive variables, are solved using a stabilized finite-element formulation. The Baldwin–  
10 Lomax model is employed for turbulence closure. Flow past an LS(1)0417 airfoil is investigated for  
11 various configurations of the leading edge cut and results are compared with those from a Clark-Y airfoil  
12 section. It is found that the configuration of the leading edge cut affects the lift-to-drag ratio ( $L/D$ ) of  
13 the parachute very significantly. The  $L/D$  value has strong implications on the flight performance of the  
14 parachute. One particular configuration results in a  $L/D$  value that is in excess of 25 at  $7.5^\circ$  angle of  
15 attack. Results are presented for other angles of attack for this configuration. Copyright © 2004 John  
16 Wiley & Sons, Ltd.

17 KEY WORDS: finite-element; ram-air parachutes; parafoil; unsteady flows; vortex shedding; turbulent  
18 flows; leading edge cut

19

### 1. INTRODUCTION

20 The need for a parachute with high lift-to-drag ratio ( $L/D$ ) for achieving longer gliding range  
21 has aroused significant research activity since late 1960s. The Rogallo wing [1] was the result  
22 of one of the earliest efforts in this direction and it housed a semi-rigid structure to maintain  
23 the leading edge shape. Soon came the idea of flexible, ram-air-inflated wing. Unlike the  
24 Rogallo wing, it could be packaged and deployed in a manner similar to traditional parachutes.  
25 The ram-air parachute consists of two low porosity fabric panels which form the upper and  
26 lower surfaces of the flying wing. The enclosed volume is partitioned into various cells by  
27 sewing fabric ribs between the upper and lower surfaces to define the aerodynamics shape.  
28 The span-wise cross-section of such a ram-air parachute is a parafoil, i.e. an airfoil with a cut  
29 on it's leading edge. Air rams in through this open cut and inflates the wing. More details

\*Correspondence to: S. Mittal, Department of Aerospace Engineering, Indian Institute of Technology, Kanpur,  
UP 208 016, India.

†E-mail: smittal@iitk.ac.in

1 on the aerodynamics of the parafoils can be found in the article by Lingard [2] and about  
 2 its applications in the paper by Nicolaidis *et al.* [3]. Many researchers [4–7] have utilized  
 3 computational methods to understand and analyze parachute systems.

4 The factors affecting the design of a parafoil namely, aerodynamics and inflation time,  
 5 are inherently conflicting with each other. A small size cut, placed close to the stagnation  
 6 point of the basic airfoil section is desirable from the point of view of good aerodynamic  
 7 performance. However, too small a leading edge cut may lead to longer, and sometimes un-  
 8 acceptable inflation time of the parachute. A large cut leads to poor aerodynamic performance  
 9 and is associated with large snatch force on the parachute during its inflation. Hence an op-  
 10 timal size of the leading edge cut is one of the key ingredients of the ram-air parachute  
 11 design.

12 Chatzikonstantinou [8] presented a coupled potential flow and finite-element analysis of  
 13 non-rigid wings. Ross [9] showed a systematic application of computational aerodynamics  
 14 methods for the design and analysis of ram-air-inflated wings using an LS(1)-0417 airfoil.  
 15 It was shown that a smaller inlet cut, located close to the stagnation point of the flow, re-  
 16 sults in higher  $L/D$ . Mittal *et al.* [10] presented an extensive 2D computational study, using  
 17 Reynolds-averaged Navier–Stokes equations, for ram-air parachutes based on Clark-Y airfoils.  
 18 The effect of the size of the leading edge cut and its orientation was investigated. Flow  
 19 separation was observed on the upper surface for all configurations of the leading edge cut.  
 20 However, the flow on the lower surface is sensitive to the configuration of the leading edge  
 21 cut.

22 The LS(1)-0417 (or GA(W)-1) airfoil [11] is associated with low cruise drag, and high  
 23 values of  $L/D$  and maximum lift coefficient, and a good behavior close to stall. With a 17%  
 24 thick section, it is a good candidate for use in ram-air parachutes. In the present study, different  
 25 configurations of the leading edge cut for this airfoil are compared and comparisons drawn  
 26 with the data for the Clark-Y airfoil. The computations are limited to the investigation of the  
 27 steady-state glide performance. Furthermore, the present effort does not incorporate the fluid–  
 28 structure interactions that might affect the aerodynamics of ram-air parachutes. A finite-element  
 29 method with the streamline-upwind/Petrov–Galerkin (SUPG) and pressure-stabilizing/Petrov–  
 30 Galerkin (PSPG) stabilization technique [12] is employed. The finite-element mesh consists  
 31 of a structured mesh close to the body and an unstructured part, generated via Delaunay’s  
 32 triangulation away from the body. This type of a grid has the ability of handling fairly complex  
 33 geometries while still providing the desired resolution close to the body to, effectively, capture  
 34 the boundary layer flow. Turbulence in the flow is modeled via the Baldwin–Lomax turbulence  
 35 model [13]. Mittal and Saxena [14, 15] employed the Baldwin–Lomax turbulence model along  
 36 with the stabilized finite-element formulation, being used in this paper, to study the flow past a  
 37 NACA 0012 airfoil. They were able to capture the phenomenon of hysteresis that is observed  
 close to the static stall of the airfoil.

39

## 2. THE GOVERNING EQUATIONS

40 Let  $\Omega \subset \mathbb{R}^{n_{sd}}$  and  $(0, T)$  be the spatial and temporal domains, respectively, where  $n_{sd}$  is the  
 41 number of space dimensions, and let  $\Gamma$  denote the boundary of  $\Omega$ . The spatial and temporal  
 42 co-ordinates are denoted by  $\mathbf{x}$  and  $t$ . The Navier–Stokes equations governing incompressible  
 43

1 fluid flow are

$$\rho \left( \frac{\partial \mathbf{u}}{\partial t} + \mathbf{u} \cdot \nabla \mathbf{u} - \mathbf{f} \right) - \nabla \cdot \boldsymbol{\sigma} = \mathbf{0} \quad \text{on } \Omega \text{ for } (0, T) \quad (1)$$

$$\nabla \cdot \mathbf{u} = \mathbf{0} \quad \text{on } \Omega \text{ for } (0, T) \quad (2)$$

Here  $\rho$ ,  $\mathbf{u}$ ,  $\mathbf{f}$  and  $\boldsymbol{\sigma}$  are the density, velocity, body force and the stress tensor, respectively.  
 3 The stress tensor is written as the sum of its isotropic and deviatoric parts:

$$\boldsymbol{\sigma} = -p\mathbf{I} + \mathbf{T}, \quad \mathbf{T} = 2\mu\boldsymbol{\varepsilon}(\mathbf{u}), \quad \boldsymbol{\varepsilon}(\mathbf{u}) = \frac{1}{2}((\nabla \mathbf{u}) + (\nabla \mathbf{u})^T) \quad (3)$$

5 where  $p$  and  $\mu$  are the pressure and viscosity. Both the Dirichlet and Neumann-type boundary conditions are accounted for. They are represented as

$$\mathbf{u} = \mathbf{g} \text{ on } \Gamma_g, \quad \mathbf{n} \cdot \boldsymbol{\sigma} = \mathbf{h} \text{ on } \Gamma_h \quad (4)$$

7 where  $\Gamma_g$  and  $\Gamma_h$  are complementary subsets of the boundary  $\Gamma$ . The initial condition on the  
 9 velocity is specified on  $\Omega$ :

$$\mathbf{u}(\mathbf{x}, 0) = \mathbf{u}_0 \quad \text{on } \Omega \quad (5)$$

11 where  $\mathbf{u}_0$  is divergence-free.

### 3. FINITE-ELEMENT FORMULATION

13 Consider a finite-element discretization of  $\Omega$  into subdomains  $\Omega^e$ ,  $e = 1, 2, \dots, n_{el}$ , where  $n_{el}$  is  
 15 the number of elements. Based on this discretization, for velocity and pressure we define the  
 finite-element trial function spaces  $\mathcal{S}_u^h$  and  $\mathcal{S}_p^h$ , and weighting function spaces  $\mathcal{V}_u^h$  and  $\mathcal{V}_p^h$ .  
 These function spaces are selected, by taking the Dirichlet boundary conditions into account,  
 17 as subsets of  $[\mathbf{H}^{1h}(\Omega)]^{n_{sd}}$  and  $\mathbf{H}^{1h}(\Omega)$ , where  $\mathbf{H}^{1h}(\Omega)$  is the finite-dimensional function space  
 over  $\Omega$ .

19 The stabilized finite-element formulation of Equations (1)–(2) is written as follows: find  
 $\mathbf{u}^h \in \mathcal{S}_u^h$  and  $p^h \in \mathcal{S}_p^h$  such that  $\forall \mathbf{w}^h \in \mathcal{V}_u^h$ ,  $q^h \in \mathcal{V}_p^h$

$$\begin{aligned} & \int_{\Omega} \mathbf{w}^h \cdot \rho \left( \frac{\partial \mathbf{u}^h}{\partial t} + \mathbf{u}^h \cdot \nabla \mathbf{u}^h - \mathbf{f} \right) d\Omega + \int_{\Omega} \boldsymbol{\varepsilon}(\mathbf{w}^h) : \boldsymbol{\sigma}(p^h, \mathbf{u}^h) d\Omega + \int_{\Omega} q^h \nabla \cdot \mathbf{u}^h d\Omega \\ & + \sum_{e=1}^{n_{el}} \int_{\Omega^e} \frac{1}{\rho} (\tau_{\text{SUPG}} \rho \mathbf{u}^h \cdot \nabla \mathbf{w}^h + \tau_{\text{PSPG}} \nabla q^h) \\ & \cdot \left[ \rho \left( \frac{\partial \mathbf{u}^h}{\partial t} + \mathbf{u}^h \cdot \nabla \mathbf{u}^h - \mathbf{f} \right) - \nabla \cdot \boldsymbol{\sigma}(p^h, \mathbf{u}^h) \right] d\Omega^e \\ & + \sum_{e=1}^{n_{el}} \int_{\Omega^e} \tau_{\text{LSIC}} \nabla \cdot \mathbf{w}^h \rho \nabla \cdot \mathbf{u}^h d\Omega^e = \int_{\Gamma_h} \mathbf{w}^h \cdot \mathbf{h} d\Gamma \end{aligned} \quad (6)$$

21

1 In the variational formulation given by Equation (6), the first three terms and the left-  
 2 hand side constitute the Galerkin formulation of the problem. The first series of element-level  
 3 integrals are the SUPG and PSPG stabilization terms added to the variational formulations  
 4 [12]. The second series of element-level integrals, based on the least-squares of the continuity  
 5 equation, are added to the formulation for numerical stability at high Reynolds numbers.  
 6 For details and definitions of the stabilization parameters, the reader may refer to our earlier  
 7 articles [12, 16].

8 Three-noded triangular elements with linear interpolation functions for, both, velocity and  
 9 pressure are employed for computations. The Baldwin–Lomax model [13] is used for turbu-  
 10 lence closure. Its implementation in the context of unstructured grids can be found in the  
 11 papers by Kallinderis [17], Mavriplis [18], and Anderson and Bonhaus [19]. A second-order-  
 12 in-time procedure, based on the generalized trapezoidal method, is used for time integration.  
 13 The non-linear equation systems resulting from the finite-element discretization of the flow  
 14 equations are solved using the Generalized Minimal RESidual (GMRES) technique [20] in  
 15 conjunction with diagonal preconditioners. The matrix-free version of the GMRES algorithm  
 16 is used which reduces the memory requirements.

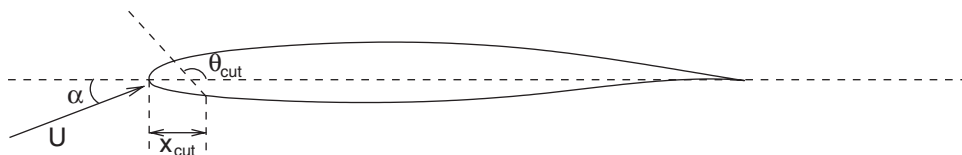
#### 17 4. PROBLEM DESCRIPTION

##### 18 4.1. The parameters

19 Figure 1 shows the schematic of the flow past a 2D-section of a ram-air parachute placed  
 20 at an angle of attack ( $\alpha$ ) to the free-stream flow. The location and size of the leading edge  
 21 cut are denoted by  $x_{\text{cut}}$  and  $\theta_{\text{cut}}$ .  $x_{\text{cut}}$  is the distance measured from the leading edge of the  
 22 airfoil along the chord length where the cut is applied and  $\theta_{\text{cut}}$  is the angle of the cut with  
 23 the chord-line. The Reynolds number ( $Re$ ) is based on the chord length ( $c$ ) of the airfoil,  
 24 free-stream velocity and viscosity of the fluid. All the values for the lift ( $C_l$ ) and drag ( $C_d$ )  
 25 coefficients and the Strouhal number, reported in this article, have been non-dimensionalized  
 26 with respect to the chord length of the clean airfoil (without the cut) and free-stream speed.

##### 27 4.2. Computational domain and finite-element mesh

28 The LS(1)0417 airfoil resides in a rectangular domain whose upstream and downstream bound-  
 29 aries are located at 5 and 11 chord lengths from the leading edge, respectively. The upper  
 30 and lower boundaries lie at 5 chord lengths each from the leading edge. The finite-element  
 31 meshes used in various computations consist of a structured triangular element mesh on the  
 32 body and an unstructured mesh generated via Delaunay's triangulation, elsewhere. This type



33 Figure 1. Flow past a ram-air parafoil: schematic.

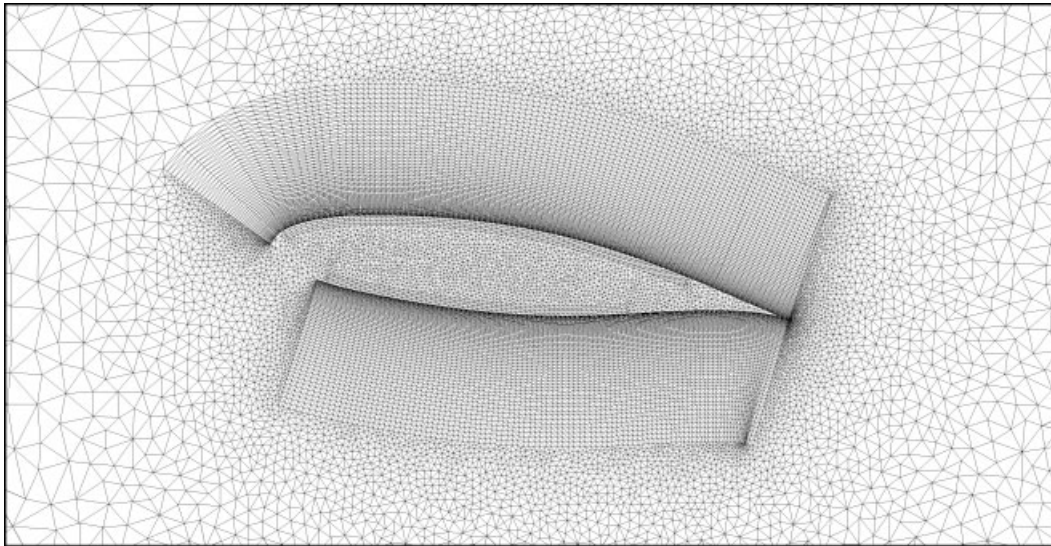


Figure 2. Close-up view of a typical finite-element mesh employed for the computations: LS(1)0417 parafoil with  $x_{\text{cut}} = 0.1c$ ,  $\theta_{\text{cut}} = 150^\circ$  and  $\alpha = 7.5^\circ$ . The mesh consists of 20 927 nodes and 41 412 triangular elements.

1 of grid has the ability of handling fairly complex geometries while still providing the de-  
 2 sired resolution close to the body to effectively capture the boundary layer flow, especially in  
 3 the context of unsteady flows. This type of a grid enables the investigation of the effect of  
 4 the various configurations of the leading edge cut and also facilitates the implementation  
 5 of Baldwin–Lomax model. A fictitious boundary is inserted in order to increase the den-  
 6 sity of nodes near the body and in the wake. The mesh is designed such that in the di-  
 7 rection normal to the wall the first element thickness is  $10^{-4}c$  so that the flow in the  
 8 boundary layer region is also captured accurately. A typical finite-element mesh is shown in  
 9 Figure 2.

#### 4.3. Boundary conditions

11 The porosity of the fabric forming the parafoil is neglected. The no-slip condition is specified  
 12 for the velocity on the parafoil surface while free-stream values are assigned for the velocity  
 13 at the upstream boundary. At the downstream boundary we specify a Neumann-type boundary  
 14 condition for the velocity that corresponds to zero viscous stress vector. On the upper and  
 15 lower surface boundaries the component of velocity normal to and the component of stress  
 16 vector along these boundaries is prescribed zero value. To account for the pressure differential  
 17 across the fabric, two sets of nodes, one for the outer and the other for the internal flow, are  
 utilized.

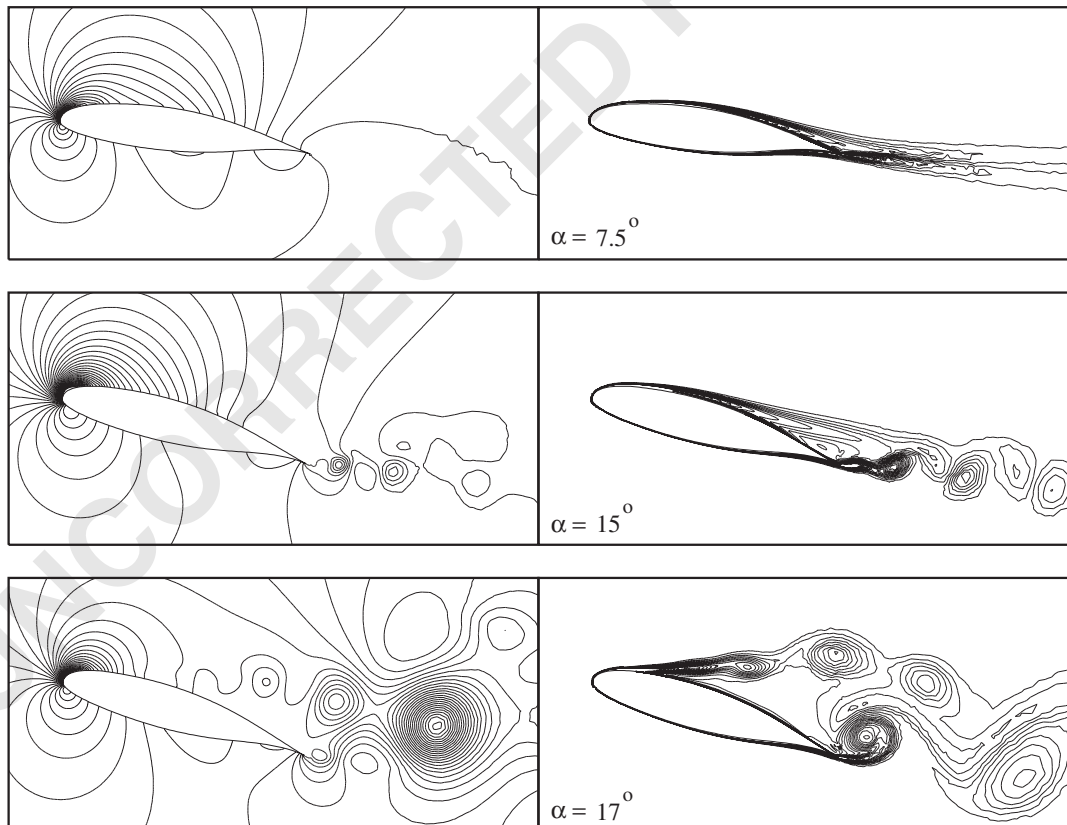
1

## 5. RESULTS

3 Most of the results presented in this paper are for turbulent flow at  $Re = 10^6$  based on the chord  
 4 of the airfoil. First, results are presented for  $Re = 10^6$  turbulent flow past a clean LS(1)0417  
 5 airfoil at various angles of attack and compared with the available experimental data. Next,  
 6 results for a baseline configuration of the leading edge cut with  $x_{\text{cut}} = 0.1c$  and  $\theta_{\text{cut}} = 135^\circ$   
 7 are presented. The effect of  $x_{\text{cut}}$  is studied by changing it to  $0.05c$  with  $\theta_{\text{cut}}$  same as the  
 8 baseline model. The effect of  $\theta_{\text{cut}}$  is investigated by comparing the baseline case with that for  
 9  $x_{\text{cut}} = 0.1c$  and  $\theta_{\text{cut}} = 150^\circ$ .

9 *5.1. Flow past a clean LS(1)0417 airfoil*

10  $Re = 10^6$  turbulent flow past a clean (without a leading edge cut) LS(1)0417 airfoil at angles  
 11 of attack,  $\alpha = 7.5, 15$  and  $17^\circ$  is computed. The finite-element mesh consists of 31 685 nodes  
 and 63 024 triangular elements and is quite similar to the one shown in Figure 2. Figure 3



13 Figure 3.  $Re = 10^6$  turbulent flow past a clean LS(1)0417 airfoil: pressure (left) and vorticity (right) fields for the fully developed flow.

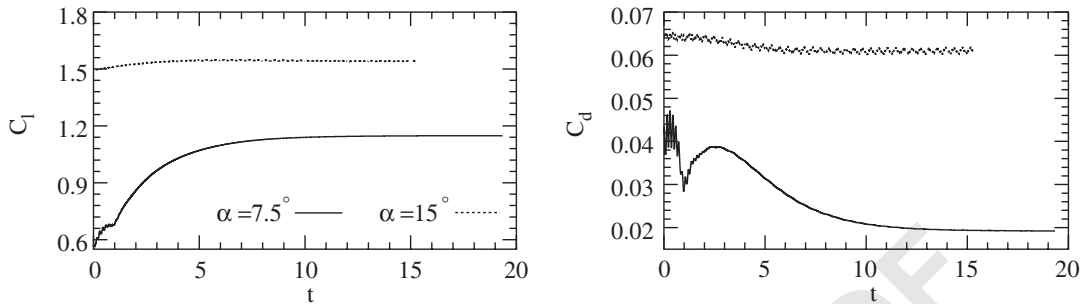


Figure 4.  $Re = 10^6$  turbulent flow past a clean LS(1)0417 airfoil: time histories of the lift and drag coefficients.

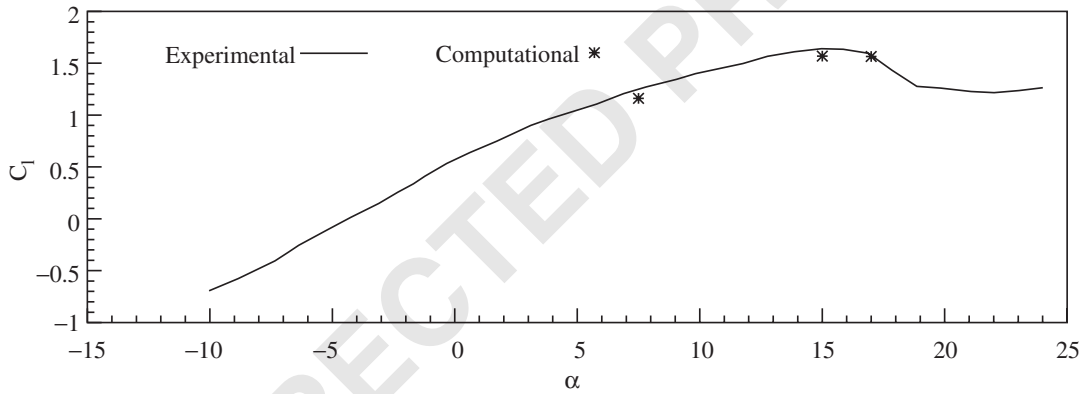


Figure 5.  $Re = 1.9 \times 10^6$  turbulent flow past a clean LS(1)0417 airfoil: variation of the lift coefficient with angle of attack. The experimental results at  $Mach = 0.15$  are from McGhee and Beasley [11].

1 shows the pressure and vorticity fields for the various angles of attack. While a steady state is  
 2 achieved by the flow for  $\alpha = 7.5^\circ$ , vortex-shedding is observed for  $\alpha = 15$  and  $17^\circ$ . For  $\alpha = 7.5^\circ$ ,  
 3 the flow separation takes place towards the trailing edge. It moves towards the leading edge  
 4 of the airfoil as  $\alpha$  increases. For all cases, the flow on the lower surface remains attached. The  
 5 time histories of the lift and drag coefficients are shown in Figure 4. The unsteadiness in the  
 6 flow for  $\alpha = 15^\circ$  can also be observed from the time variation in the aerodynamic coefficients.  
 7 The variation of the time-averaged  $C_l$  with  $\alpha$  is shown in Figure 5 along with the experi-  
 8 mental data from McGhee and Beasley [11]. Good agreement with the experimental results  
 9 is observed. The flatness in the  $C_l$  vs  $\alpha$  at large angles of attack, as opposed to a sharp drop,  
 10 points to the good stall characteristics of this airfoil. The time-averaged values of the lift  
 11 and drag coefficients and corresponding  $C_l/C_d$  ratios are shown in Table I. The  $(C_l)_{max}$  for  
 12 this airfoil is, approximately, 1.6. At large  $\alpha$ , although  $C_l$  sustains a high value,  $C_d$  increases  
 13 significantly. This results in a low value of  $C_l/C_d$  at large  $\alpha$ . It appears that the optimal  $\alpha$ ,  
 for maximum  $C_l/C_d$ , might be close to  $7.5^\circ$ . This, of course, needs more calculations to be

Table I.  $Re = 10^6$  turbulent flow past a clean LS(1)0417 airfoil for various angles of attack: time-averaged values of the aerodynamic coefficients.

Case	$\alpha$ (deg)	$C_l$	$C_d$	$C_l/C_d$
1	7.5	1.148	0.019	60.42
2	15	1.567	0.061	25.69
3	17	1.561	0.119	13.12

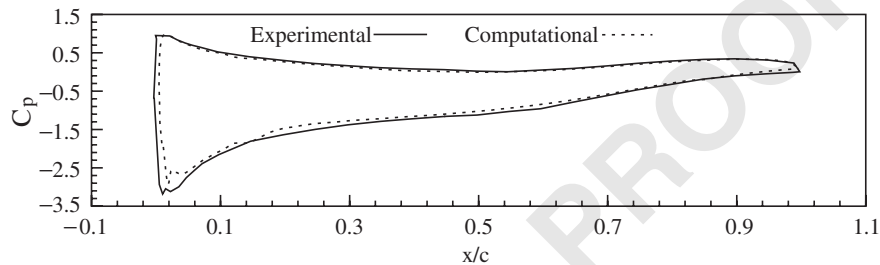


Figure 6.  $Re = 6.3 \times 10^6$  turbulent flow past a clean LS(1)0417 airfoil: chord-wise variation of the pressure coefficient for  $\alpha = 7.5^\circ$ . The experimental results at  $Mach = 0.15$  and  $\alpha = 8.02^\circ$  are from McGhee and Beasley [11].

1 established. Figure 6 shows the chord-wise variation of the pressure coefficient for  $\alpha = 7.5^\circ$  and  
 2  $Re = 6.3 \times 10^6$ . Also shown in the figure is the experimental data from McGhee and Beasley  
 3 [11]. The good agreement between the results from present computations and already existing  
 4 data establishes confidence in these results. Similar comparisons for the Clark-Y airfoil can  
 5 be found in Reference [10].

### 5.2. $Re = 10^6$ turbulent flow past a parafoil with leading edge cut

7 5.2.1.  $x_{cut} = 0.1c$ ,  $\theta_{cut} = 135^\circ$ . 2D turbulent flow ( $Re = 10^6$ ) past a parafoil based on LS(1)0417  
 8 airfoil with  $x_{cut} = 0.1c$  and  $\theta_{cut} = 135^\circ$  at angles of attack,  $\alpha = 7.5$  and  $15^\circ$  is presented. To  
 9 incorporate the effect of the cut, flow inside as well as outside the parafoil is simulated. The  
 10 sharp corners at the leading edge cut are expected to result in flow separation and the mesh is  
 11 sufficiently refined in such regions to provide adequate resolution. The vorticity and pressure  
 12 fields corresponding to the peak values of the lift coefficient for the fully developed unsteady  
 13 flow are shown in Figure 7. While the flow for a clean airfoil at  $\alpha = 7.5^\circ$  is associated with  
 14 mild separation on the upper surface, the parafoil with a leading edge cut experiences an  
 15 unsteady flow that separates on the upper surface right at the leading edge. This shows that  
 16 the leading edge cut changes the flow, qualitatively. Its effect cannot be estimated from the  
 17 flow past a clean airfoil. The flow at  $\alpha = 15^\circ$  suffers even more separation and unsteadiness.  
 18 Interestingly, the flow on the lower surface remains attached, despite the leading edge cut. It  
 19 will later be shown in this paper that at lower  $\alpha$ , flow separation is observed on the lower  
 20 surface of the parafoil. The pressure on the inner surface of the parafoil assumes an almost  
 21 constant value that is equal to the stagnation pressure.

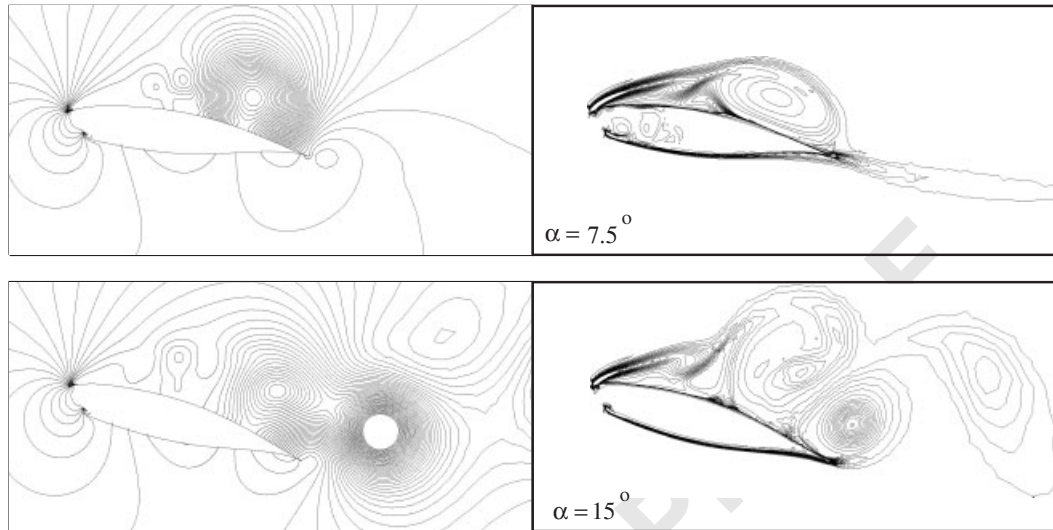


Figure 7.  $Re = 10^6$  turbulent flow past LS(1)0417 parafoil with  $x_{cut} = 0.1c$  and  $\theta_{cut} = 135^\circ$ : pressure (left) and vorticity (right) fields for the fully developed unsteady flow. The flow pictures correspond to the time instant when the lift coefficient achieves its peak value.

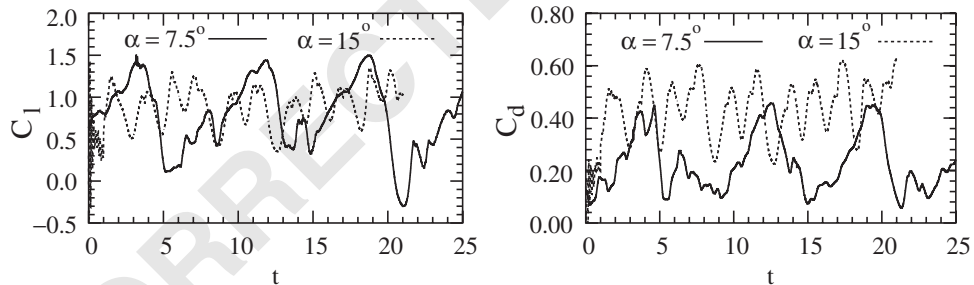


Figure 8.  $Re = 10^6$  turbulent flow past LS(1)0417 parafoil with  $x_{cut} = 0.1c$  and  $\theta_{cut} = 135^\circ$ : time histories of the lift and drag coefficients.

1 The time histories of the lift and drag coefficients are shown in Figure 8. The peak value  
 2 of the lift coefficient corresponds to the instant when the large clockwise rotating vortex is  
 3 fully developed and is located on the upper surface of the parafoil causing an increased suction.  
 4 During each cycle of lift coefficient a clockwise rotating vortex is shed from the upper  
 5 surface and a counter-clockwise rotating vortex is shed from the lower surface at the trailing  
 6 edge. The time averaged aerodynamic coefficients are listed in Tables II and III. It is ob-  
 7 served that, compared to a clean airfoil at  $\alpha = 7.5^\circ$ , the time-averaged lift coefficient decreases  
 8 by about 22% while the drag coefficient increases by more than ten-folds. Also shown in  
 9 Table II is the data for the parafoil based on the Clark-Y airfoil [10]. For  $x_{cut} = 0.1c$  and  
 10  $\theta_{cut} = 135^\circ$ , the performance from the two geometries for  $\alpha = 7.5^\circ$  is quite comparable. For  
 11  $\alpha = 15^\circ$ , the performance of the parafoil is not good.

Table II.  $Re = 10^6$ ,  $\alpha = 7.5^\circ$  turbulent flow past a ram-air parafoil with LS(1)0417 and Clark-Y sections for various configurations of the leading edge cut: time-averaged values of the aerodynamic coefficients.

Case	$x_{cut}$	$\theta_{cut}$	LS(1)0417			Clark-Y [10]		
			$C_l$	$C_d$	$C_l/C_d$	$C_l$	$C_d$	$C_l/C_d$
1	No cut	No cut	1.148	0.019	60.42	1.38	0.0204	67.65
2	$0.1c$	$135^\circ$	0.894	0.245	3.65	0.99	0.29	3.41
3	$0.05c$	$135^\circ$	0.887	0.237	3.74	1.09	0.19	5.74
4	$0.1c$	$150^\circ$	0.880	0.034	25.88	1.01	0.21	4.81

Table III.  $Re = 10^6$ ,  $\alpha = 15^\circ$  turbulent flow past a ram-air parafoil based on LS(1)0417 section for various configurations of the leading edge cut: time-averaged values of the aerodynamic coefficients.

Case	$x_{cut}$	$\theta_{cut}$	$C_l$	$C_d$	$C_l/C_d$
1	$0.10c$	$135^\circ$	1.122	0.511	2.20
2	$0.05c$	$135^\circ$	1.103	0.482	2.29
3	$0.10c$	$150^\circ$	1.264	0.448	2.82

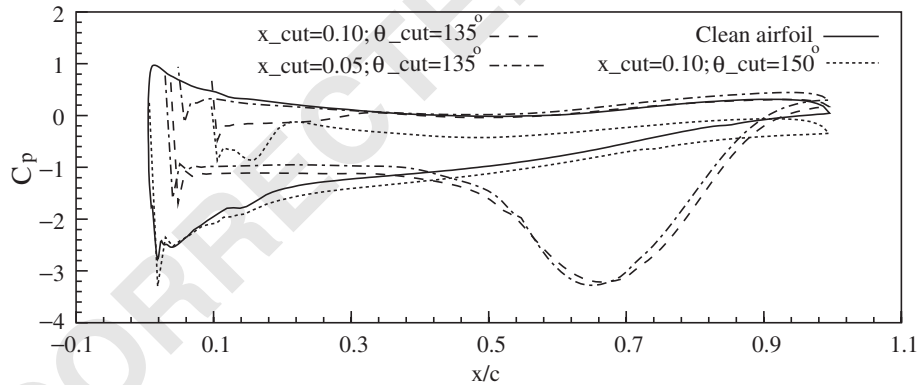


Figure 9.  $Re = 10^6$ ,  $\alpha = 7.5^\circ$  turbulent flow past LS(1)0417 parafoil: chord-wise distribution of pressure coefficient for different configurations of the leading edge cut. The pictures correspond to the time instant when the lift coefficient achieves its peak value.

1 Figure 9 shows the variation of the pressure coefficient on the outer surface of the parafoil  
 2 corresponding to the peak value of the lift coefficient. Also shown in the figure is the  $C_p$   
 3 distribution for the clean airfoil for  $\alpha = 7.5^\circ$ . The leading edge cut results in a significant loss  
 4 in lift because of two major effects. For a clean airfoil the region on the upper surface near  
 5 the leading edge is associated with high suction and contributes significantly to the total lift.  
 6 The cut leads to an effective loss in the suction and the size of the body at the leading edge.  
 7 This results in loss of lift and increase in drag. In addition, the leading edge cut is responsible  
 for the flow separation that results in further deterioration of performance.

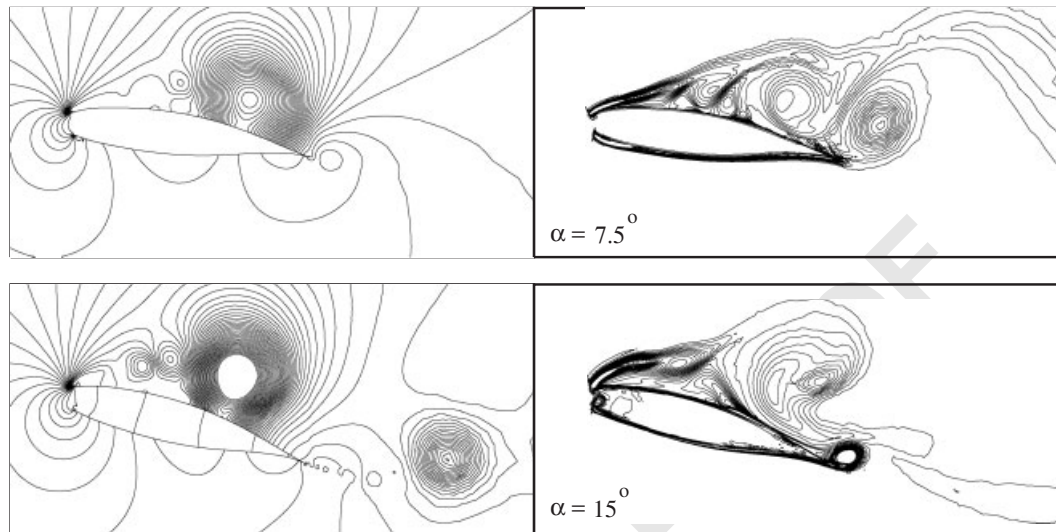


Figure 10.  $Re = 10^6$  turbulent flow past LS(1)0417 parafoil with  $x_{cut} = 0.05c$  and  $\theta_{cut} = 135^\circ$ : pressure (left) and vorticity (right) fields for the fully developed unsteady flow. The flow pictures correspond to the time instant when the lift coefficient achieves its peak value.

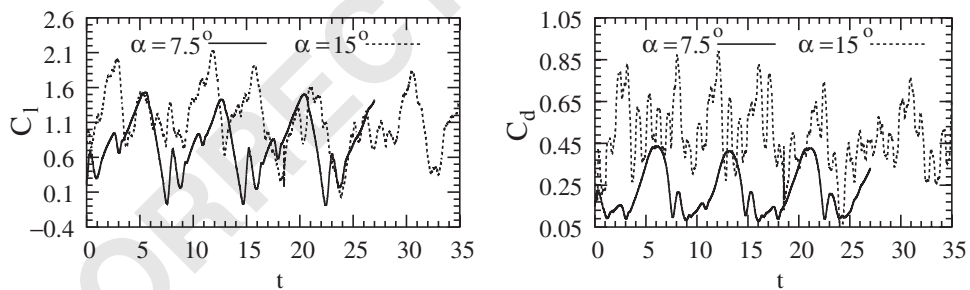


Figure 11.  $Re = 10^6$  turbulent flow past LS(1)0417 parafoil with  $x_{cut} = 0.05c$  and  $\theta_{cut} = 135^\circ$ : time histories of the lift and drag coefficients.

- 1 5.2.2.  $x_{cut} = 0.05c$ ,  $\theta_{cut} = 135^\circ$ . To investigate the effect of  $x_{cut}$ ,  $\theta_{cut}$  is maintained at  $135^\circ$
  - 3 while  $x_{cut}$  is reduced to  $0.05c$ . A reduction in the leading edge cut is expected to improve the
  - 5 aerodynamic performance. The vorticity and pressure fields corresponding to the peak values
  - 7 of the lift coefficient for the fully developed unsteady flow at  $\alpha = 7.5$  and  $15^\circ$  are shown in
  - 9 Figure 10. These flow pictures appear to be analogous to the ones for  $x_{cut} = 0.1c$ : the flow
- separates near the trailing-edge on the lower surface and, right at the leading edge on the upper surface. The time histories of the lift and drag coefficients are shown in Figure 11. From Tables II and III it can be noted that the time-averaged values of coefficients for both the sections are almost similar, with  $x_{cut} = 0.05c$  faring slightly better in terms of the  $C_l/C_d$

1 ratio. With the Clark-Y section the  $x_{\text{cut}} = 0.05c$  results in a significantly better performance  
 2 than the parafoil section with  $x_{\text{cut}} = 0.1c$ . In the case of a Clark-Y airfoil, compared to the  
 3 section with  $x_{\text{cut}} = 0.1c$ ,  $0.05c$  causes a significant reduction in flow separation at the lower  
 4 surface. However, in the present case, with the LS(1)0417 section, the flow does not appear  
 5 to be sensitive to changes in  $x_{\text{cut}}$ .

5.2.3.  $x_{\text{cut}} = 0.1c$ ,  $\theta_{\text{cut}} = 150^\circ$ . The effect of a change in  $\theta_{\text{cut}}$  with respect to the baseline  
 7 configuration of the leading edge cut is investigated. While  $x_{\text{cut}}$  is maintained at  $0.1c$ ,  $\theta_{\text{cut}}$  is  
 8 increased to  $150^\circ$ . The flow figures corresponding to the peak value of the lift coefficient for  
 9 the fully developed unsteady flow are shown in Figure 12. Compared to the previous cases, a  
 10 significantly lower vortical activity is observed for  $\alpha = 7.5^\circ$ . In fact, the flow is quite similar  
 11 to that observed for a clean airfoil. From Table II we observe that this configuration of the  
 12 parafoil results in a much lower value of the drag coefficient. As a result, the  $C_l/C_d$  for this  
 13 section is in excess of 25. From Figure 9 it can be observed that amongst all the leading  
 14 edge configurations considered in this study, the present one yields  $C_p$  distribution that is  
 15 closest to the one for a clean airfoil. The  $C_p$  distribution on the upper surface (suction side)  
 16 is very similar to that for the clean airfoil. On the lower surface, the presence of separation  
 17 bubble results in lower pressure as compared to a clean airfoil. These results indicate that  
 18 this configuration of the parafoil is expected to give very good glide performance and that,  
 19 as compared to  $x_{\text{cut}}$ ,  $\theta_{\text{cut}}$  is a more useful design parameter for this airfoil section.

*Flows at various  $\alpha$ :* Encouraged by the characteristics of this configuration of the parafoil at  
 21  $\alpha = 7.5^\circ$ , computations have been carried out for other angles of attack. Figure 12 shows the  
 22 vorticity and pressure fields for the fully developed unsteady flow, for various  $\alpha$ , corresponding  
 23 to the time instant when the lift coefficient attains a peak value. The flow behavior, as the  
 24  $\alpha$  increases, is quite interesting. For  $\alpha = 0^\circ$ , the flow is attached on the upper surface but  
 25 separates, and then reattaches, on the lower surface. Also, compared to the upper surface, the  
 26 boundary layer is much thicker on the lower surface. As  $\alpha$  is increased, the boundary layer on  
 27 the upper surfaces thickens and the point of flow separation moves upstream from the trailing  
 28 edge towards the leading edge, gradually. At the same time, the boundary layer on the lower surface  
 29 becomes thinner and more stable. In fact, the time-averaged  $C_d$  for  $\alpha = 5^\circ$  is lower than that  
 30 at  $\alpha = 0^\circ$ . At  $\alpha = 10^\circ$  the flow is quite stable with very low level of unsteadiness, primarily  
 31 on the upper surface. At  $\alpha = 15^\circ$ , the flow separates right at the leading edge on the upper  
 32 surface. However, the flow on the lower surface is associated with a thin, attached boundary  
 33 layer.

Table IV shows the time-averaged aerodynamic coefficients for various  $\alpha$ . The maximum  
 35 value of  $C_l/C_d$  is achieved for  $\alpha \sim 5^\circ$ . Ross [9] found that for a parafoil with  $x_{\text{cut}} = 0.04c$ ,  $C_l/C_d$   
 36 is maximum at  $\alpha \sim 4^\circ$ . For  $\alpha \leq 10^\circ$ , the flow separation is mild which results in reasonably  
 37 low drag and high  $C_l/C_d$ . At larger  $\alpha$  the flow on the upper surface separates at the leading  
 38 edge causing a huge increase in  $C_d$ . The time histories of the lift and drag coefficients for  
 39 various  $\alpha$  are shown in Figure 13. It is interesting to note that the level of unsteadiness is  
 40 lowest for  $\alpha$  between  $5$  and  $10^\circ$ . In fact, at  $\alpha = 10^\circ$ , the flow is almost steady. These results  
 41 indicate that the present configuration of the parafoil holds enormous promise for its practical  
 42 usage for  $\alpha \leq 10^\circ$ .

*Convergence study:* The flow at  $\alpha = 7.5^\circ$  for the parafoil with  $x_{\text{cut}} = 0.1c$  and  $\theta_{\text{cut}} = 150^\circ$  is  
 43 subjected to a convergence study with respect to spatial and temporal resolution. This flow  
 44 is associated with mild unsteadiness and is expected to be quite sensitive to the resolution.

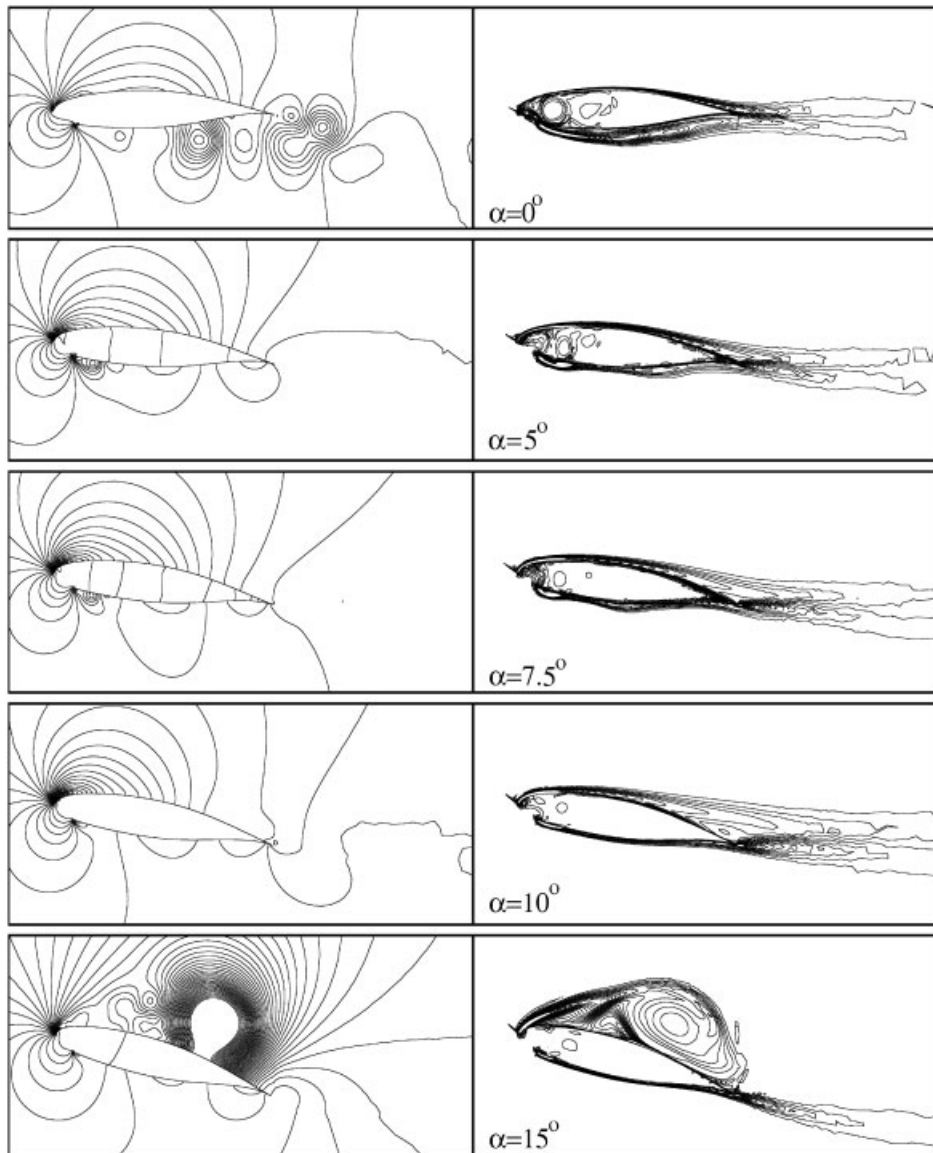


Figure 12.  $Re = 10^6$  turbulent flow past LS(1)0417 parafoil with  $x_{cut} = 0.1c$  and  $\theta_{cut} = 150^\circ$ : pressure (left) and vorticity (right) fields for the fully developed unsteady flow. The flow pictures correspond to the time instant when the lift coefficient achieves its peak value.

- 1 Computations are carried out with three finite-element meshes of different levels of resolution. The details of the meshes and a summary of the time-averaged aerodynamic coefficients along with their rms values are given in Table V. A close-up view of Mesh M1 is shown in Figure 2.
- 3 Meshes M2 and M3 are more refined close to the parafoil but very similar to M1, far away.

Table IV.  $Re = 10^6$  turbulent flow past the LS(1)0417 parafoil with  $x_{cut} = 0.1c$  and  $\theta_{cut} = 150^\circ$  for various  $\alpha$ : time-averaged values of the aerodynamic coefficients.

Case	$\alpha$ (deg)	$C_l$	$C_d$	$C_l/C_d$
1	0	0.314	0.036	8.72
2	5	0.746	0.022	32.75
3	7.5	0.880	0.034	25.88
4	10	0.876	0.056	15.54
5	12	0.950	0.236	4.02
6	15	1.264	0.448	2.82

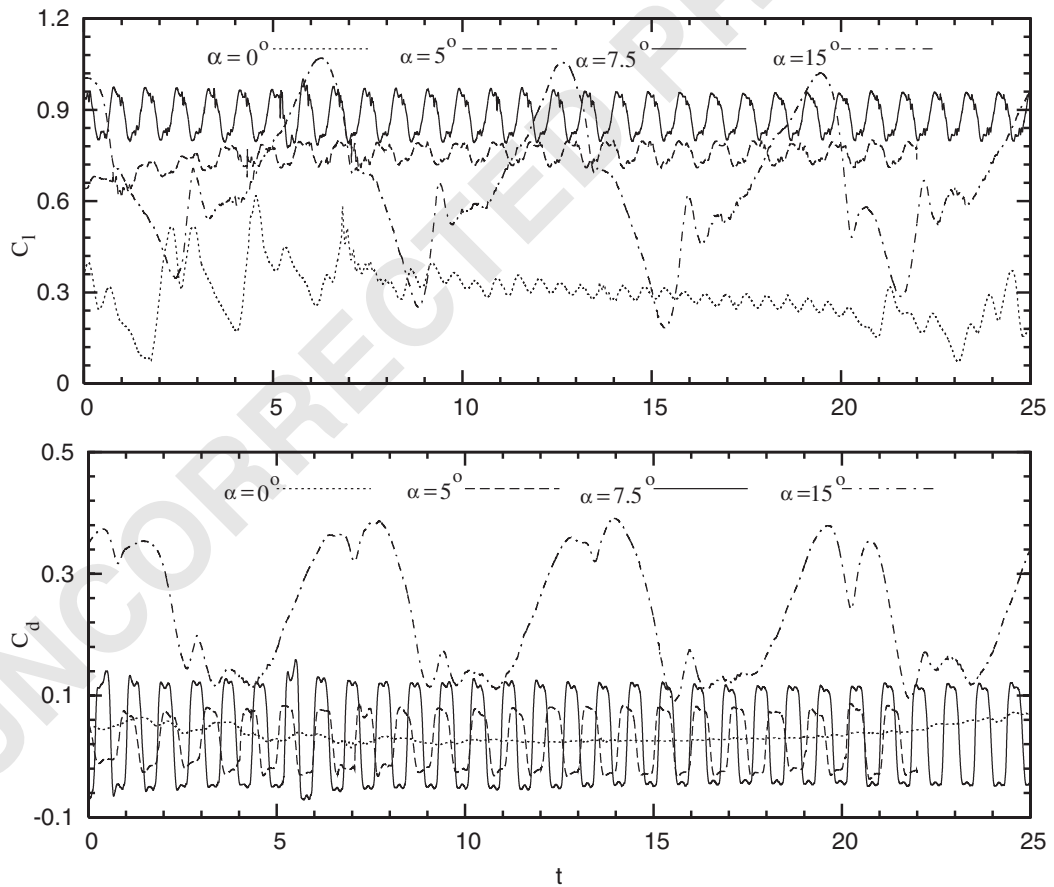


Figure 13.  $Re = 10^6$  turbulent flow past LS(1)0417 parafoil with  $x_{cut} = 0.1c$  and  $\theta_{cut} = 150^\circ$ : time histories of the lift and drag coefficients.

Table V.  $Re = 10^6$ ,  $\alpha = 7.5^\circ$  turbulent flow past the LS(1)0417 parafoil with  $x_{cut} = 0.1c$  and  $\theta_{cut} = 150^\circ$  for various finite-element meshes: time-averaged and rms values of the aerodynamic coefficients.

Case	Mesh	nodes	elements	$C_l$	$C_d$	$C_l/C_d$	$(C_l)_{rms}$	$(C_d)_{rms}$
1	M1	20 927	41 412	0.880	0.032	27.25	0.058	0.075
2	M2	36 044	71 606	0.914	0.035	26.04	0.068	0.105
3	M3	64 402	1 28 137	0.963	0.035	27.27	0.070	0.121

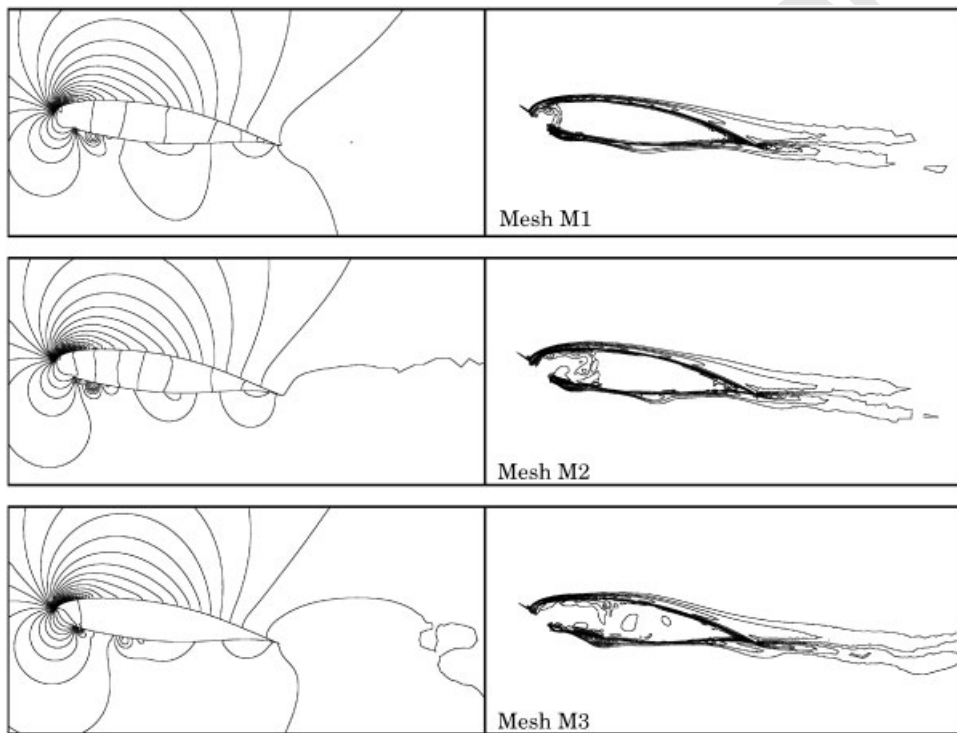


Figure 14.  $Re = 10^6$ ,  $\alpha = 7.5^\circ$  turbulent flow past LS(1)0417 parafoil with  $x_{cut} = 0.1c$  and  $\theta_{cut} = 150^\circ$ : pressure (left) and vorticity (right) fields for the fully developed unsteady flow computed with three finite-element meshes of different levels of refinement.

- 1 While the time step for Mesh M1 is  $10^{-3}$ , it is  $10^{-4}$  for Mesh M3. The vorticity and pressure
- 2 fields for the three meshes are shown in Figure 14. It is observed that the flows computed
- 3 with the three meshes are in good agreement. As expected, the higher resolution close to the
- 4 parafoil results in slightly larger unsteadiness in the flow as reflected by the rms values of the
- 5 aerodynamic coefficients. However, the difference in the  $C_l/C_d$  values from the various meshes
- 6 is less than 5%. Mesh refinement studies for other values of  $\alpha$  where the unsteadiness is higher
- 7 have shown that those flows are less sensitive to resolution. The present computations provide

1

## 6. CONCLUDING REMARKS

Results have been presented for computation of two-dimensional turbulent flow past a ram-air parachute with a leading edge cut. Flow past a LS(1)0417 airfoil, without a leading edge cut, for  $\alpha = 7.5^\circ$  results in an attached flow. The computed results compare well with the experimental data. In general, the sharp corners at the leading edge cut cause flow separation and unsteadiness in the flow even at low  $\alpha$ . Compared to a clean airfoil, significant loss in lift and increase in drag, is observed. The flow inside the parafoil cell remains almost stagnant resulting in a high value of pressure that is responsible for giving the parafoil its shape. Even though the clean airfoil gives a reasonable  $C_l/C_d$  for  $\alpha = 15^\circ$ , the parafoil with any configuration of the leading edge cut does not give acceptable performance.

11 The configuration of the leading edge cut has a strong influence on the lift-to-drag ratio. It is found that a cut at 10% chord and  $150^\circ$  angle results in significantly better performance than the other cases that were studied. For  $\alpha$  in the range of  $5-10^\circ$ , this configuration of the cut causes very little change to the basic flow past the clean airfoil and very high value of  $C_l/C_d$  is achieved. It is observed that compared to  $x_{\text{cut}}$ , the parameter  $\theta_{\text{cut}}$  has a larger effect on the performance of the parafoil.

17 Although the performance of the clean LS(1)0417 and Clark-Y airfoils are comparable, the situation is quite different for certain configurations of the cut. While the configuration with  $x_{\text{cut}} = 0.05c$  and  $\theta_{\text{cut}} = 135^\circ$  yields better performance for the Clark-Y section, it is  $x_{\text{cut}} = 0.1c$  and  $\theta_{\text{cut}} = 150^\circ$  that works best with the LS(1)0417 airfoil. The optimal leading edge cut depends on the airfoil section being considered. It appears that the LS(1)0417 section holds more promise for use in ram-air parachutes. More work needs to be done to confirm this observation. The present computations are two-dimensional and assume that the parafoil retains its prescribed shape. Wind-tunnel tests and/or computations that incorporate fluid-structure interactions and three-dimensional effects are needed to address these issues.

## REFERENCES

- 27 1. Rogallo FM. NASA research on flexible wings. *International Congress of Subsonic Aeronautics*, New York, NY, U.S.A. April 1967.
- 29 2. Lingard JS. The aerodynamics of gliding parachutes. *AIAA Paper* 86-2427-CP, 1986.
- 31 3. Nicolaides JD, Speelman III RJ, Menard GLC. A review of parafoil applications. *Journal of Aircraft* 1970; 7:423-431.
- 33 4. Aliabadi SK, Garrard WL, Kalro V, Mittal S, Tezduyar TE, Stein KR. Parallel finite element computations of the dynamics of large ram air parachutes. *AIAA Paper* 95-1581, *13th Aerodynamic Decelerator and Systems Conference*, Clearwater, FL, 1995; 278-293.
- 35 5. Garrard WL, Tezduyar TE, Aliabadi SK, Kalro V, Luker J, Mittal S. Inflation analysis ram air inflated gliding parachutes. *AIAA Paper* 95-1565, *13th Aerodynamic Decelerator and Systems Conference*, Clearwater, FL, 1995; 186-198.
- 37 6. Benney RJ, Stein KR. Computational fluid-structure interaction model for parachute inflation. *Journal of Aircraft* 1996; 33:730-736.
- 39 7. Strickland JH, Higuchi H. Parachute aerodynamics: an assessment of prediction capability. *Journal of Aircraft* 1996; 33:709-749.
- 41 8. Chatzikonstantinou T. Numerical analysis of three-dimensional non-rigid wings. *AIAA-89-0907*, 1989.
- 43 9. Ross JC. Computational aerodynamics in the design and analysis of ram-air-inflated wings. *AIAA Paper* 93-1228 RAeS/AIAA, *12th Aerodynamic Decelerator Systems Technology Conference and Seminar*, London, U.K., 1993.
- 45 10. Mittal S, Saxena P, Singh A. Computation of two-dimensional flows past ram-air parachutes. *International Journal for Numerical Methods in Fluids* 2001; 35:643-667.
- 47 11. McGhee RJ, Beasley WD. Low-speed aerodynamic characteristics of a 17-percent thick airfoil section designed for general aviation applications. *Technical Report NASA TND-7428*, NASA Langley Research Center, 1973.
- 49

- 1 12. Tezduyar TE, Mittal S, Ray SE, Shih R. Incompressible flow computations with stabilized bilinear and linear  
3 equal-order-interpolation velocity–pressure elements. *Computer Methods in Applied Mechanics and Engineering*  
1992; **95**:221–242.
- 5 13. Baldwin B, Lomax H. Thin layer approximation and algebraic turbulence model for separated turbulent flows.  
*AIAA Paper 78-257, AIAA 16th Aerospace Sciences Meeting*, Huntsville, AL, 1978.
- 7 14. Mittal S, Saxena P. Prediction of hysteresis associated with the static stall of an airfoil. *AIAA Journal* 2000;  
**38**:933–935.
- 9 15. Mittal S, Saxena P. Hysteresis in flow past a NACA 0012 airfoil. *Computer Methods in Applied Mechanics*  
*and Engineering* 2001; **191**:2179–2189.
- 11 16. Mittal S. On the performance of high aspect-ratio elements for incompressible flows. *Computer Methods in*  
*Applied Mechanics and Engineering* 2000; **188**:269–287.
- 13 17. Kallinderis Y. Algebraic turbulence modeling for adaptive unstructured grids. *AIAA Journal* 1992; **30**:631–639.
- 15 18. Mavriplis DJ. Turbulent flow calculations using unstructured and adaptive meshes. *International Journal for*  
*Numerical Methods in Fluids* 1991; **13**:1131–1152.
- 17 19. Anderson WK, Bonhaus DL. An implicit upwind algorithm for computing turbulent flows on unstructured grids.  
*Computers and Fluids* 1994; **23**:1–21.
20. Saad Y, Schultz M. GMRES: a generalized minimal residual algorithm for solving nonsymmetric linear systems.  
*SIAM Journal on Scientific and Statistical Computing* 1986; **7**:856–869.